Flexible Transparent Electrodes Formed from Template-Patterned Thin-Film Silver

Sihai Luo,* Enkui Lian, Jiali He, and John C. deMello*

Template-patterned, flexible transparent electrodes (TEs) formed from an ultrathin silver film on top of a commercial optical adhesive – Norland Optical Adhesive 63 (NOA63) – are reported. NOA63 is shown to be an effective base-layer for ultrathin silver films that advantageously prevents coalescence of vapor-deposited silver atoms into large, isolated islands (Volmer-Weber growth), and so aids the formation of ultrasmooth continuous films. 12 nm silver films on top of free-standing NOA63 combine high, haze-free visible-light transparency ($T \approx 60\%$ at 550 nm) with low sheet-resistance ($\mathcal{R}_s \approx 16\ \Omega\ \text{sq}^{-1}$), and exhibit excellent resilience to bending, making them attractive candidates for flexible TEs. Etching the NOA63 base-layer with an oxygen plasma before silver deposition causes the silver to laterally segregate into isolated pillars, resulting in a much higher sheet resistance ($\mathcal{R}_s > 8 \times 10^6\ \Omega\ \text{sq}^{-1}$) than silver grown on pristine NOA63 . Hence, by selectively etching NOA63 before metal deposition, insulating regions may be defined within an otherwise conducting silver film, resulting in a differentially conductive film that can serve as a patterned TE for flexible devices. Transmittance may be increased (to 79% at 550 nm) by depositing an antireflective layer of Al_2O_3 on the Ag layer at the cost of reduced flexibility.

1. Introduction

The growing demand for flexible optoelectronic devices has generated a need for compliant, haze-free, stable, transparent electrodes (TEs) on thin, plastic substrates that exhibit high transparency and low sheet-resistance combined with excellent resilience under repeated flexing at bending diameters down to a few mm.[1,2] Transmittance and sheet-resistance requirements vary between applications: for instance, capacitive and resistive touch-panels require sheet resistances of a few hundred ohms per square ($\Omega\ \text{sq}^{-1}$) at 80% – 90% transmittance, while (current-driven) solar cells and organic light-emitting diodes require sheet resistances of 10–50 $\Omega\ \text{sq}^{-1}$ at similar transmittance levels.[3] For photodetectors, a sheet resistance of < 100 $\Omega\ \text{sq}^{-1}$ and a transmittance of > 50% is needed for high bandwidth and responsivity, but in addition, the electrode should exhibit an extremely low surface roughness to avoid the formation of conductive shunts that would otherwise increase leakage currents and reduce detectivity.[4,5] More generally, low surface roughness is needed for many thin-film devices to minimize pinholes and shunts that are known to accelerate device degradation.[6] Thermotherapy pads – which use moderate, localized heating to treat musculoskeletal pain, oedema, muscle spasm, and various other medical conditions – require sheet resistances of around 20 $\Omega\ \text{sq}^{-1}$,[7] together with haze-free optical transmittance > 50% to permit noninvasive visual inspection of treatment areas.

Beyond their physical properties, it is advantageous from a manufacturing perspective if the TEs can be deposited directly onto a flexible substrate (as opposed to it being necessary to first deposit onto a rigid substrate and then transfer to a flexible substrate afterward).[8] It is also beneficial if the TE material can be patterned down to the few-micron level without recourse to time-consuming, costly, and environmentally harmful photolithography.[9]

Indium tin oxide (ITO) remains the dominant transparent conductor for rigid applications due to its good chemical and thermal stability, and its excellent transmittance (T) versus sheet resistance ($\mathcal{R}_s$) trade-off characteristics. However, the scarcity and high cost of indium have created a strong demand for cheaper, more sustainable alternative TE materials.[10] The need to replace ITO is even more acute for flexible applications due to its tendency to crack when flexed, which leads to large irreversible increases in sheet resistance.[11] Many materials systems have been suggested as candidate TEs for flexible substrates, including conducting polymers,[12] single-walled carbon nanotubes (SWCNTs),[13] graphene,[14] metal oxides,[11] metal nanowires,[15] ultra-thin metal films (UTMFs)[16] and multilayer structures based on UTMFs and metal oxides.[17] However, as

S. Luo, E. Lian, J. C. deMello
Department of Chemistry
Norwegian University of Science and Technology (NTNU)
Trondheim 7491, Norway
E-mail: sihai.luo@ntnu.no; john.demello@ntnu.no
J. He
Department of Materials Science and Engineering
Norwegian University of Science and Technology (NTNU)
Trondheim 7491, Norway

outlined in Appendix S1 and Table S1 of the Supporting Information, each material system has different strengths and weaknesses in relation to the criteria listed above.

Ultrathin metal films of thickness < 20 nm offer a particularly simple approach to making highly flexible, transparent electrodes, using mature mass-production processes such as thermal evaporation, e-beam evaporation, and sputtering. UTMFs stand-out for their favorable combination of simple preparation, efficient materials usage, excellent compliancy, and good T versus $\mathcal{R}_s$ trade-off characteristics. Fragility of the UTMF electrodes and relatively high root-mean-squared (RMS) surface roughness values (of several nm) have been identified as potential limitations,[11] but as we show in this manuscript these issues can be overcome by an appropriate choice of substrate. The key challenge in fabricating UTMF electrodes is to suppress the natural tendency of thin metal films to segregate into isolated clusters (leading to high sheet resistance),[18] which can be achieved through a judicious choice of the substrate material (or surface treatment thereof) and by carefully controlling the deposition conditions. The best trade-off characteristics are obtained by using doped metal films or seed layers of a second metal to induce nucleation. Optimized 7-nm nickel-doped silver films on polyethylene terephthalate (PET), for instance, have been reported to exhibit a sheet resistance of 19 Ω sq^{-1} at 79% average transmittance (400 – 700 nm),[19] only slightly worse than the best results reported for pristine (unflexed) ITO on PET. Further improvements in the trade-off characteristics may be obtained by sandwiching the doped **M**etal between antireflective **D**ielectric layers in a so-called **DMD** configuration.[17] Sheet resistances as low as 18.6 Ω sq^{-1} at 88.4% average transmittance (400 – 700 nm) have been reported for a ZnO/Cu-doped Ag/Al$_2$O$_3$ structure on a PET substrate.[20] However, DMD structures are susceptible to crack formation in the oxide layers and delamination at the dielectric/metal interfaces when they are repeatedly flexed at low bending diameters, limiting their use in flexible applications.[16,21]

In this manuscript, we report flexible TEs formed from ultrathin (< 20 nm) films of silver on top of a commercially sourced optical adhesive – Norland Optical Adhesive 63 (NOA63). NOA63 is a thermoset resin formed from a mixture of mercapto esters and the cross-linking agent triallyl isocyanuarte that under ultraviolet (UV) light exposure forms a fused polymer matrix with high transparency from 380 to 3000 nm.[22,23] NOA63 is widely used for bonding glass-, quartz- and sapphire-based optical elements and for bonding glass to metal. For TE applications, it has the benefits of excellent optical transparency in the visible/near-infra-red (Vis/NIR) range, good mechanical flexibility, and good chemical stability. Thin-film NOA63 has previously been used as a host matrix for silver nanowire-based TEs,[24,25] while nano-embossed NOA63 has been used as an antireflective adhesion layer between PET and ultrathin silver, resulting in enhanced Vis/NIR transmittance characteristics relative to PET/Ag films.[26] Polyimide-coated NOA63 has also been used as a substrate for TEs formed from gold microgrids and PEDOT:PSS.[27]

Here we show that NOA63 acts as an effective base layer for ultrathin silver films that advantageously prevents coalescence of vapor-deposited metal atoms into large discrete islands (Volmer-Weber growth), and so aids the formation of ultra-smooth continuous films needed for TE applications. We show that ≈12 nm films of silver on top of NOA63 combine high, haze-free transparency with low sheet resistance, and exhibit excellent resilience to bending, making them attractive candidates for flexible TEs. We further show that etching the NOA63 base layer with an oxygen plasma prior to silver deposition causes the silver layer to laterally segregate into isolated pillars, resulting in extremely poor in-plane conduction compared to silver grown on pristine NOA63. Hence, by selectively etching NOA63 prior to metal deposition, it is possible to define insulating regions within a layer of otherwise conducting silver and so obtain a differentially conducting silver layer that can serve as a patterned TE for optoelectronics. The selectively-etched NOA63 acts as a template that directs the growth of the silver during deposition, and we, therefore, refer to the patterning procedure as "template patterning".

For convenience, in the remainder of this paper, we use the abbreviations "p-OA" and "e-OA" to denote **p**ristine (unetched) and **e**tched NOA63 optical adhesive (OA), respectively; "OA" without any prefix denotes NOA63 in either form. Bilayers of NOA63 and silver are denoted "OA/Ag" or "OA/Ag(x)" where "x" is an integer denoting the approximate thickness d_{Ag} of the silver layer in nm (as determined by a quartz crystal microbalance). Trilayers of NOA63, silver, and alumina are denoted "OA/Ag/Al$_2$O$_3$" or "OA/Ag(x)/Al$_2$O$_3$(y)" where x and y refer to the respective thicknesses of silver and alumina in nm.

2. Results

Figure 1 shows the key steps for fabricating the template-patterned OA/Ag TEs. A clean glass slide is used as a supporting substrate and coated with octadecyltrichlorosilane (OTS) – a self-assembled monolayer (SAM) that facilitates later detachment of the OA/Ag TE from the glass slide (Figure 1-i). Optical adhesive of approximate thickness 10 μm is spin-cast on top of the SAM and cured under 365-nm UV light (Figure 1-ii). A shadow mask is then placed against the upper surface of the OA-coated glass, and the exposed parts of the OA are partially etched using an oxygen plasma (Figure 1-iii). Next, the mask is removed, and an ultrathin layer of silver (< 20 nm) is deposited uniformly over the entire substrate by electron beam deposition (Figure 1-iv), with the silver spontaneously forming regions of low sheet resistance above pristine OA and regions of high sheet resistance above etched OA. In the final step, the patterned OA/Ag electrode is peeled away from the substrate, facilitated by the weak adhesion between NOA63 and the outward-facing alkyl tail of OTS, yielding a free-standing flexible TE (Figure 1-v).

The described procedure has several advantages over conventional methods for micropatterning metals such as shadow-mask evaporation and photolithography. In shadow-mask evaporation, gradual furring or deformation of the mask may occur due to adhesion of evaporated material, leading to a loss of patterning fidelity and a need for regular mask maintenance.[28,29] In the method described here, a shadow mask is used prior to metal deposition to spatially confine the oxygen plasma, but the mask is not damaged by the plasma treatment and does not require cleaning after use. Plasma etching moreover occurs isotropically, and therefore allows patterning right-up to the edge of the shadow mask, avoiding the blurring and shadowing artefacts that are associated with shadow-mask evaporation.

Photolithographic patterning of metals involves slow and costly multistep processes that have a substantial environmental
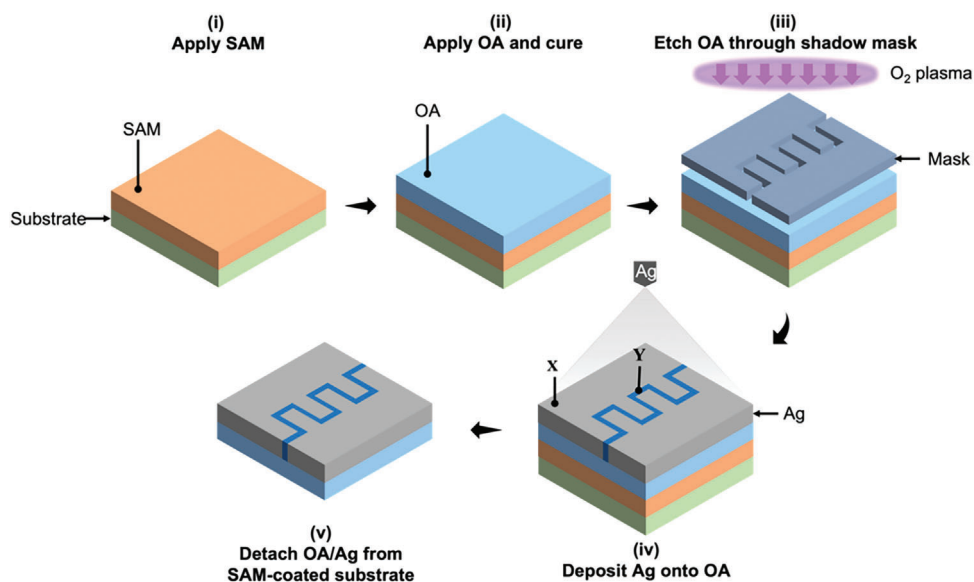
2300058 (2 of 11)

**ADVANCED
SCIENCE NEWS**

www.advancedsciencenews.com

**ADVANCED
MATERIALS**

www.advmat.de

Figure 1. Schematic showing the fabrication procedure for patterned OA/Ag TEs. A self-assembled monolayer (SAM) of octadecyltrichlorosilane (OTS) is deposited on a clean glass slide (i). A 10-µm layer of the optical adhesive (OA) NOA63 is spin-cast on top of the SAM and cured under UV light (ii). The OA is selectively exposed to an oxygen plasma by means of a shadow mask (iii). The shadow mask is removed, and an ultrathin layer of silver (< 20 nm) is uniformly coated over the full area of the substrate by electron-beam deposition, yielding conducting regions (X) above pristine OA and insulating regions (Y) above etched OA (iv). The Ag-coated OA film is detached from the glass substrate by peeling, yielding a free-standing, flexible TE (v).

impact in terms of both energy consumption and hazardous reagent use.[9] Fabrication of the patterned OA/Ag electrodes reported here by contrast involves just four simple process steps (OA deposition, UV-curing, selective oxygen plasma treatment, and mask-free metal deposition), making it easier to implement than photolithographic patterning, with a correspondingly lower environmental impact. Unlike shadow-mask evaporation and photolithography, at the end of the OA/Ag patterning procedure, the TE surface is composed entirely of silver in both the conducting and the insulating regions. Hence, the electrodes may have useful applications in bioelectronics, where the well documented antibacterial properties of silver can be expected to prevent biofouling compared to a traditionally patterned electrode with exposed regions of substrate. (See for instance Ref. [30] where higher rates of microbial growth are reported for uncoated plastic substrates than for silver-coated substrates).

Figure 2a,b shows tapping-mode Atomic Force Microscope (AFM) images of p-OA on glass before and after depositing 12 nm of silver. The RMS surface roughness $\Re$ of the bare p-OA film was ≈0.2 nm, substantially lower than the 0.6 nm roughness of the underlying glass substrate. Hence, p-OA acts as an effective planarising layer that is capable of smoothing out surface asperities on glass. Comparing Figure 2a,b it can be seen that the surface roughness increased only slightly after silver deposition (to 0.3 nm), and remained much lower than that of the glass substrate. The p-OA/Ag film was much smoother than an equivalent silver film deposited directly on glass (see Figure S1b, Supporting Information), where the widely reported tendency of silver atoms to diffuse across the surface of the glass and aggregate into isolated islands [18] resulted in a measured $\Re$-value of 1.9 nm. The p-OA/Ag(12) sample was also substantially smoother than a sample of commercially sourced pristine ITO on glass ($\Re = 2.2$ nm, see Figure S1a, Supporting Information).

Figure 2c,d shows equivalent AFM images for e-OA on glass. Oxygen plasma treatment of the bare OA film led to a substantial increase in the surface roughness to 11.8 nm (Figure 2c), with the observed morphology resembling a series of separate but closely spaced vertical pillars of typical width 60 – 90 nm. The observed increase in the surface roughness of the NOA63 is consistent with a previous report, in which partially cured NOA63 on a rigid acrylic substrate underwent wrinkling when subjected to (low pressure) oxygen plasma treatment as a result of stress induced by the colliding oxygen ions.[31] The same pillared structure was broadly maintained after depositing 12 nm of silver, albeit with a reduction in $\Re$ to ≈7.5 nm. As we show below, the spatial separation of the silver-coated e-OA pillars leads to extremely poor in-plane conductivity, with the fragmented silver effectively behaving as an insulator over macroscopic length scales. For thin Ag films in the approximate range 10 – 20 nm, the local morphology of the silver layer (continuous versus fragmented) is primarily determined by the morphology of the underlying OA. Hence, if the OA is selectively etched prior to metal deposition, it has a strong templating influence on the growth of the silver layer, causing the silver to spontaneously segregate into continuous (conducting) regions above pristine NOA63 and fragmented (insulating) regions above etched NOA63.

The formation of conducting and insulating regions above pristine and etched NOA63, respectively, is a consequence of strong bonding between silver and the sulfur atoms in the thiol groups of NOA63, see Figure S2, Supporting Information and Refs. [32,33]. Bonding between the OA substrate and the deposited metal atoms leads to the formation of shallow metallic islands with a small contact angle and large width-to-height ratio, and lowers the diffusion of Ag atoms along the NOA63 surface, reducing the tendency of adjacent islands to coalesce into the larger (taller) islands associated with volmer-weber growth.[18]
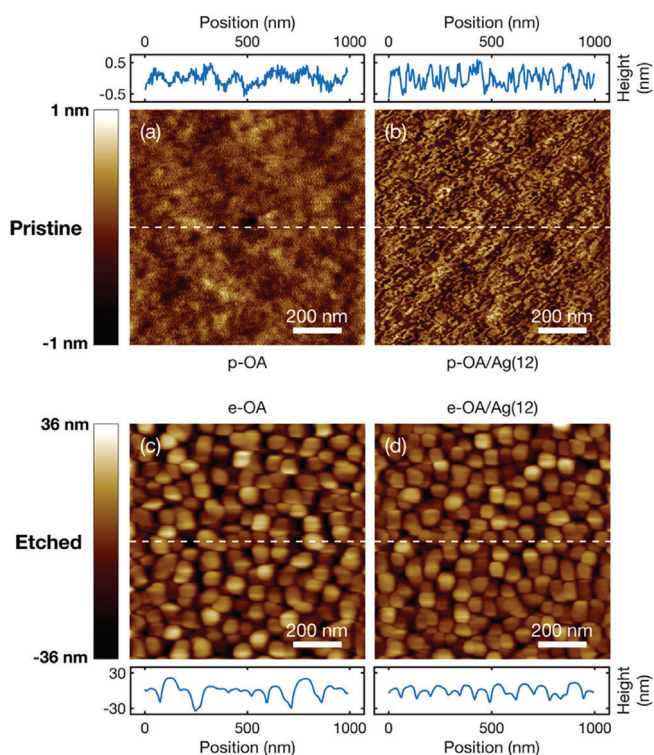
ADVANCED
SCIENCE NEWS

www.advancedsciencenews.com

ADVANCED
MATERIALS

www.advmat.de

Figure 2. Atomic Force Microscope (AFM) images of pristine (a,b) and etched (c,d) NOA63 optical adhesive before and after deposition of a 12 nm layer of silver. The main images show 1 μm by 1 μm AFM images obtained in tapping mode, while the plots show corresponding line profiles along the paths indicated by the horizontal, white dotted lines. The root-mean-squared roughness values before and after silver deposition were 0.2 nm and 0.3 nm for p-OA and 11.8 nm and 7.5 nm for e-OA. For p-OA/Ag(12) the silver forms an ultrasmooth, continuous layer, while for e-OA/Ag(12) it fragments into isolated pillars.

Hence, for deposition onto smooth p-OA, strong substrate-metal bonding encourages the formation of smooth, dense films that exhibit percolation (and therefore low sheet resistance) at low film thicknesses. For deposition onto rough e-OA/Ag, strong substrate-metal bonding leads to a base layer of silver atoms that follows the undulations of the substrate, which in turn induces voids and grain boundaries in the deposited silver film that disrupt in-plane conductivity, leading to high sheet resistance.[34]

The visual appearance of the OA/Ag films is affected by the nature of the underlying OA layer as can be seen from **Figure 3**a, which shows a photograph of 12 nm silver on top of selectively etched OA. The e-OA/Ag region on the left side of the substrate is visibly darker (less transparent) than the p-OA/Ag region on the right side. The transmittance spectra of p-OA/Ag(12) and e-OA/Ag(12) are shown in Figure 3b. The p-OA/Ag(12) sample had a peak transmittance of 67.7% at 432 nm, which fell monotonically to 45.2% at 730 nm, giving it a slight blue tint under indoor lighting conditions. The e-OA/Ag(12) sample had a somewhat flatter transmittance spectrum across the visible wavelength range, varying from a peak of 49.9% at 443 nm to 35.7% at 730 nm, giving it a fairly neutral grey coloration. The p-OA/Ag(12) and e-OA/Ag(12) samples had mean transmittances across the visible spectrum (380 – 730 nm) of 58.7% and 43.9%,

respectively, and both exhibited high optical clarity with no sign of haze to the eye. In Appendix S2 of the Supporting Information, we show that the lower transmittance and flatter spectral profile of the e-OA/Ag(12) sample is consistent with the high interfacial roughness at the OA/Ag and Ag/air boundaries, which leads to increased, broadly wavelength-independent absorptive losses within the silver layer. Additional photographs showing the transparency and flexibility of the NOA63/Ag electrodes are shown in Figure 3c,d.

Figure 4a shows the OA/Ag sheet resistance $\mathcal{R}_s$ versus etching time t for a fixed Ag film thickness of 12 nm. $\mathcal{R}_s$ values were determined using a four-point probe configuration with a probe-spacing of 1.27 mm. Using a pristine OA film as the base layer ($t = 0$ min), a low sheet resistance of 16 Ω sq^{-1} was measured. Subjecting the OA to an oxygen plasma treatment prior to silver deposition resulted in a dramatic increase in the measured sheet resistance of the OA/Ag films, with $\mathcal{R}_s$ changing to 145, 6×10^{10} and $> 1 \times 10^{13}$ Ω sq^{-1}. after 5, 10, and 20 mins of etching, respectively (see Methods section in Supporting Information for etching conditions). Hence, 10 mins of etching was sufficient to render the OA/Ag electrodes highly insulating relative to pristine OA/Ag. The high sheet resistance of silver on e-OA is attributable to the fragmented nanomorphology of the metal films, which leads to insulating voids between pillars (see Figure 2d). (We note that this high sheet resistance was maintained even when the e-OA/Ag electrode was compressively flexed, with the samples showing no appreciable change in sheet resistance at bending diameters down to 3 mm, see Figure S3a, Supporting Information. The e-OA/Ag sheet resistance was also unaffected by the extended application of a 1.5 V cm^{-1} external field, see Figure S3b, Supporting Information).

The highly resistive nature of nano-fragmented silver films has previously been reported by Boysen et al.,[35] who noted that ≈400 nm silver films grown by atomic layer deposition (ALD) from a N-heterocyclic carbene-based silver precursor exhibited extremely high sheet resistances due to fragmentation of the silver into isolated domains, while ≈650 nm films deposited under the same conditions exhibited sheet resistances of < 1 Ω sq^{-1} due to the formation of a continuous network of silver atoms. (Note, these films were not transparent due to the high film thicknesses).

The open markers In Figure 4b show the measured sheet resistance versus Ag thickness for a set of p-OA/Ag samples with d_{Ag} values from 0 to 40 nm. With 1 nm of Ag, an extremely high $\mathcal{R}_s$ value of $> 5.8 \times 10^9$ Ω sq^{-1} was measured – close to the value of 3.3×10^{10} Ω sq^{-1} measured for an uncoated p-OA film. Progressively increasing d_{Ag} from 1 to 12 nm caused a very sharp drop in the sheet resistance of the p-OA/Ag films, with $\mathcal{R}_s$ falling to 16 Ω sq^{-1} at $d_{Ag} = 12$ nm. However, increasing the Ag thickness beyond 12 nm had a comparatively weak effect on the sheet resistance, with $\mathcal{R}_s$ decreasing to 3 Ω sq^{-1} at $d_{Ag} = 40$ nm. The initial many orders of magnitude drop in $\mathcal{R}_s$ up to $d_{Ag} = 12$ nm is consistent with the progressive development of a percolating network on the surface of the p-OA as more silver is deposited, while the slow decrease beyond 12 nm is attributable to a gradual densification of the silver film above percolation.[36] High-resolution SEM images of 8 nm and 12 nm p-OA/Ag films are shown in Figure S4, Supporting Information. The 8 nm image is suggestive of an incompletely formed metal film with substantial voids
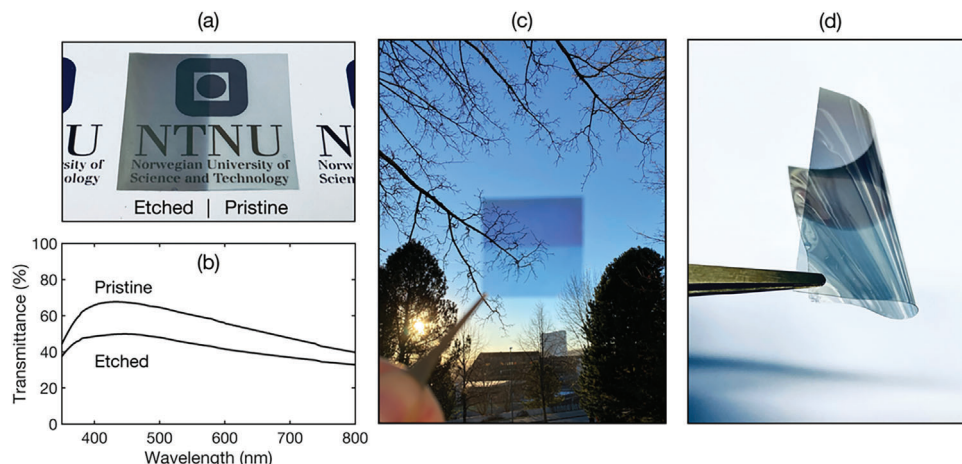
**ADVANCED
SCIENCE NEWS**

www.advancedsciencenews.com

**ADVANCED
MATERIALS**

www.advmat.de

Figure 3. a) Photographs showing 12 nm Ag on selectively etched NOA63. b) Transmittance spectra for 12-nm Ag on pristine and etched NOA63. c,d) Photographs showing the transparency and flexibility of the OA/Ag(12) patterned TEs; darker regions correspond to Ag above etched NOA63.

to interrupt percolation, while the 12 nm image is consistent with a fully percolated film.

The closed markers in Figure 4b show the measured sheet resistance versus Ag thickness for an equivalent set of e-OA/Ag samples, prepared using a common etch time of 10 min. With 1 nm of Ag, the measured $\mathcal{R}_s$ value of 1.3×10^{10} Ω sq^{-1} was

again extremely high. However, compared to the p-OA/Ag samples, increasing d_{Ag} to 12 nm caused a much smaller reduction in the sheet resistance to $\approx 8.2 \times 10^6$ Ω sq^{-1}. Increasing the silver thickness from 12 to 20 nm, by contrast, caused a very substantial drop in sheet resistance, with $\mathcal{R}_s$ falling to 66 Ω sq^{-1} at $d_{Ag} =$ 20 nm. Further increasing d_{Ag} to 40 nm caused a small reduction
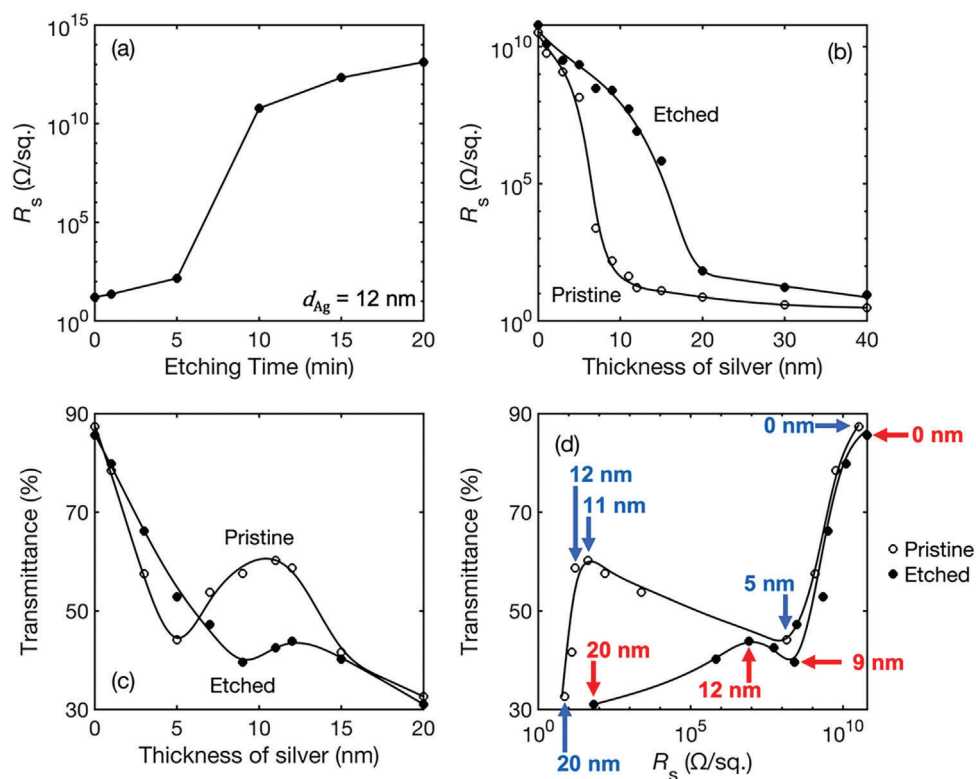

Figure 4. a) Sheet resistance versus oxygen plasma etching time for a fixed silver thickness of 12 nm; etching times of 10 mins or more yielded highly resistive silver films. b,c) Sheet resistance $\mathcal{R}_s$ and mean transmittance $\bar{T}$ (from 380 to 730 nm) versus silver thickness for pristine and etched NOA63, using a fixed etching time of 10 min. d) Mean transmittance $\bar{T}$ versus sheet resistance $\mathcal{R}_s$ for pristine and etched NOA63, using data from (b) and (c); blue and red annotations indicate the Ag film thickness on pristine and etched NOA63, respectively. Relative standard deviations for the measured sheet resistances were in the range $1 - 10\%$ for $\mathcal{R}_s$ values < 100 MΩ sq^{-1}, increasing to $\approx 60\%$ for the highest measured sheet resistance of 5.6 GΩ sq^{-1}.

2300058 (5 of 11)

in sheet resistance to ≈ 9 Ω sq^{-1}. The slow drop in $\mathcal{R}_s$ up to $d_{Ag} = 12$ nm is attributable to the column-like morphology of the underlying e-OA layer, which enforces fragmentation of the silver and so maintains a high sheet resistance. Between $d_{Ag} = 12$ nm and $d_{Ag} = 20$ nm, the deposited Ag atoms start to bridge the gaps between the columns, resulting in a rapid drop in sheet resistance. When d_{Ag} reaches 20 nm, a percolating layer of silver has been established, and the small reductions in sheet resistance thereafter are attributable to densification of the percolated film. Figure S5, Supporting Information shows AFM images for e-OA/Ag samples with 12 and 40 nm of silver, respectively. At $d_{Ag} = 12$ nm, the pillared structure that impedes in-plane conduction is clearly evident. At $d_{Ag} = 40$ nm, however, the silver layer has been planarized (with a greatly reduced surface roughness of 0.8 nm), and the corresponding AFM image shows no trace of the pillared structure of the underlying e-OA layer.

Figure 4c shows the average transmittance $\bar{T}$ in the (visible) spectral range 380 to 730 nm for p-OA/Ag and e-OA/Ag samples with d_{Ag} values from 0 to 20 nm. The p-OA/Ag samples showed a strong nonmonotonic dependence on silver thickness, with $\bar{T}$ falling from 87.3% at $d_{Ag} = 0$ nm to 44.1% at $d_{Ag} = 5$ nm, then rising to 60.2% at $d_{Ag} = 11$ nm, and then falling to 32.6% at $d_{Ag} = 20$ nm. The e-OA/Ag samples showed similar but less pronounced behavior, with $\bar{T}$ falling from 85.6% at $d_{Ag} = 0$ nm to 39.6% at $d_{Ag} = 9$ nm, then rising to 43.9% at $d_{Ag} = 12$ nm, and then falling to 31% at $d_{Ag} = 20$ nm. For d_{Ag} values $>= 7$ nm, higher average transmittances were measured for the p-OA/Ag films than for the e-OA/Ag films, with the difference being largest at $d_{Ag} = 9$ nm: 57.6% versus 39.6%.

The nonmonotonic dependence of $\bar{T}$ on d_{Ag} is due to substantial changes in the transmittance spectra of the OA/Ag films. The Vis/NIR optical properties of vapor-deposited thin silver films have previously been explained in terms of a near constant background permittivity from high energy inter-band Ag transitions plus an admixture of localized and delocalised plasmonic modes, which change in relative strength as the Ag thickness changes.[37] For thin Ag films the main plasmonic mode is a localized mode due to isolated islands of silver, while for thick films the main mode is a delocalized (Drude-type) mode due to extended regions of linked silver. Close to percolation, both these modes contribute to the observed optical spectra, together with additional localized plasmonic modes related to the nanostructure of the metal film [38] The contributions from these different modes change substantially as d_{Ag} increases from 0 to 20 nm, causing substantial changes in the transmittance spectra as shown in Figure S6, Supporting Information, which in turn account for the observed nonmonotonic dependence of $\bar{T}$ on d_{Ag}. The increase in transmittance in going from $d_{Ag} = 5$ nm to 11 nm is consistent with a reduction in absorption due to localized plasmonic modes as the amount of deposited material increases. We note that Park et al. have previously reported copper-doped silver films that showed a narrow range of thicknesses below 5 nm over which the transmittance and thickness were positively correlated (i.e., an increase in film thickness led to an increase in transmittance), and likewise attributed the behavior to excitation at low film thicknesses of a localized surface plasmon resonance.[39]

Figure 4d shows $\bar{T}$ versus $\mathcal{R}_s$ for the p-OA/Ag and e-OA/Ag films. Owing to the nonmonotonic dependence of $\bar{T}$ on d_{Ag}, the curves deviate from the usual trade-off behavior for TEs, in which a reduction in $\mathcal{R}_s$ always comes at the expense of a drop in $\bar{T}$.[40] For the case of the p-OA/Ag samples, conventional trade-off behavior is observed for very thin silver coatings up to ≈ 5 nm, with $\bar{T}$ and $\mathcal{R}_s$ falling from 87.3% and 3.3×10^{10} Ω sq^{-1} at $d_{Ag} = 0$ nm to 44.1% and 1.4×10^8 Ω sq^{-1} at $d_{Ag} = 5$ nm. However, further increases in d_{Ag} up to 11 nm can be seen to cause a substantial increase in $\bar{T}$ to 60.2% accompanied by a sharp decrease in $\mathcal{R}_s$ to 43 Ω sq^{-1}. For d_{Ag} values greater than 11 nm, conventional trade-off behavior is again observed with $\bar{T}$ and $\mathcal{R}_s$ decreasing to 32.6% and 7 Ω sq^{-1} at $d_{Ag} = 20$ nm. From the data shown in Figure 4d, d_{Ag} values of 11 or 12 nm would be the most appropriate choices for generic TE applications since thinner films with $d_{Ag} < 11$ nm deliver objectively worse performance, while thicker films with $d_{Ag} > 12$ nm have substantially lower transmittance for only a small improvement (reduction) in sheet resistance. For most applications, $d_{Ag} = 12$ nm would be preferred over $d_{Ag} = 11$ nm since a slight reduction in transmittance from 60.2% to 58.7% would typically be an acceptable cost for a 2.7-fold reduction in sheet resistance from 43 to 16 Ω sq^{-1}.

The e-OA/Ag samples also show conventional trade-off behavior for thin and thick Ag coatings, plus a narrow range of intermediate Ag thicknesses in which the transmittance and sheet resistance are negatively correlated. From $d_{Ag} = 0$ nm to 9 nm, $\bar{T}$ and $\mathcal{R}_s$ fall from 85.6% and 6.2×10^{10} Ω sq^{-1} to 39.6 % and 2.6×10^8 Ω sq^{-1}. From 9 nm to 12 nm, $\bar{T}$ increases to 43.9%, while $\mathcal{R}_s$ decreases to 8.2×10^6 Ω sq^{-1}. And, for d_{Ag} values greater than 12 nm, $\bar{T}$ and $\mathcal{R}_s$ both show a continuous decrease to 31% and 66.4 Ω sq^{-1} at $d_{Ag} = 20$ nm. It can be seen from Figure 4b,c that the properties of e-OA/Ag films with thick Ag layers approach those of the equivalent p-OA/Ag films in agreement with the AFM image of Figure S5b, Supporting Information, which shows a smooth continuous layer of silver when $d_{Ag} = 40$ nm.

At $d_{Ag} = 12$ nm (the preferred choice for p-OA/Ag films), the $\mathcal{R}_s$ values for the pristine and etched films are 16 and 8.2×10^6 Ω sq^{-1} respectively, while the mean transmittances are 58.7 and 43.9%. Hence, p-OA/Ag(12) acts as a high-performance TE, while e-OA/Ag(12) acts as an insulator. (See also Figure S7, Supporting Information, which shows conductive AFM measurements for p-OA/Ag(12) and e-OA/Ag(12), together with comparative measurements for bare glass and indium tin oxide (ITO) coated glass).

By selectively etching the OA layer prior to silver deposition, it is possible to define insulating regions within an otherwise conductive layer of silver, with the insulating regions being easily identified visually due to their substantially lower transmittance (for Ag thicknesses between 7 and 15 nm). Photographs of some patterned OA/Ag(12) TEs with varying feature sizes are shown in Figure S8, Supporting Information. In all cases, the conducting and insulating regions are clearly distinguishable by eye. The sharpness of the interface between the conducting and insulating regions is determined by the choice of the shadow mask, see Figure S9, Supporting Information. Using a rigid shadow mask allows vertical gaps to exist between the mask and the substrate, leading to ingress of the oxygen plasma into the shadow regions and unwanted broadening of the e-OA/p-OA interface. The extent of the broadening is influenced by the etching time, with longer etches resulting in a more diffuse p-OA/e-OA
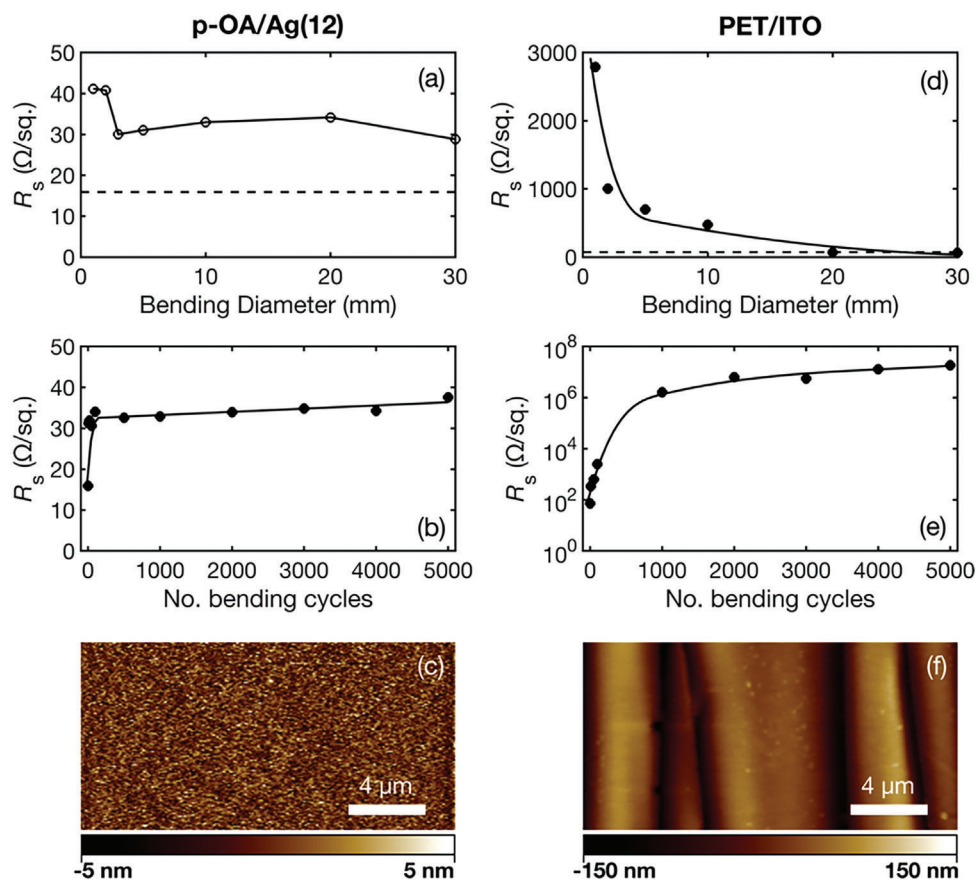
2300058 (6 of 11)

Figure 5. a) Sheet resistance $\mathcal{R}_s$ versus bending diameter D_b for a set of p-OA/Ag(12) films that have been subjected to single bends of differing curvature; the dotted horizontal line shows the sheet resistance of an unbent p-OA/Ag(12) sample. b) Sheet resistance $\mathcal{R}_s$ versus number N of bending cycles for a single p-OA/Ag(12) sample undergoing repeated bending at a fixed bending diameter of $D_b = 3$ mm. c) AFM image showing a section of the p-OA/Ag(12) sample from (b) after completion of 5000 bending cycles. The surface roughness after 5000 bending cycles was 1.2 nm compared to 0.3 nm before. d–f) Equivalent data for PET/ITO TEs with $\bar{T} = 78\%$ and $\mathcal{R}_s \approx 70\ \Omega\ \mathrm{sq}^{-1}$.

interface. This can be seen in Figures S9a,d, Supporting Information, which show interfacial widths of ≈10 nm and 50 nm after 10- and 20-mins of etching, respectively.

Using a conformal mask that attaches directly to the substrate avoids ingress of the oxygen plasma into the shadow regions, resulting in sharp interfaces that are unaffected by the duration of etching. This may, for example, be achieved using a patterned photoresist as a shadow mask (see Figure S9b,e, Supporting Information), although using a photoresist introduces the unwanted complexity of photolithographic processing into the process flow. A preferable approach that retains the simplicity of the OA/Ag patterning procedure is to use an elastomeric mask that can reversibly attach to the OA substrate under applied pressure via induced dipole-dipole attraction (London dispersion forces). Figure S9c,f, Supporting Information, show the result of using a polydimethylsiloxane (PDMS) shadow mask to confine the oxygen plasma. Sharp sub-10-nm interfaces are obtained after 10- and 20-mins of etching, comparable to those obtained using the photoresist. PDMS and related elastomers have the further advantage of being compatible with laser patterning, and hence allowing for rapid prototyping of the OA/Ag electrodes.

Figure 5a shows the sheet resistance $\mathcal{R}_s$ for a set of p-

OA/Ag(12) films that have been subjected to single bends of differing curvature, with the bending diameter D_b varying from 30 mm to 1 mm. The dotted horizontal line denotes (for comparison) the $16\ \Omega\ \mathrm{sq}^{-1}$ sheet resistance $\mathcal{R}_s^\infty$ of an unbent p-OA/Ag(12) film. Single bends of $D_b = 30, 20, 10, 5$ and 3 mm resulted in an approximate doubling of the sheet resistance to $31 \pm 2\ \Omega\ \mathrm{sq}^{-1}$, while sharper bends of $D_b = 2$ and 1 mm resulted in a further increase to ≈41 $\Omega\ \mathrm{sq}^{-1}$. Figure 5b shows the measured sheet resistance versus number of bending cycles for repeated bends at a fixed bending diameter of 3 mm. After 10 bends an approximate doubling of the sheet resistance from 16 to 31 Ω sq^{-1} was observed. Further bending, however, resulted in only a slight increase in the sheet resistance, with $\mathcal{R}_s$ reaching 38 Ω/sq. after 5000 bending cycles. Figure 5c shows an AFM image of the sample after the completion of the bending regime. The image resembles the AFM image of an unbent sample shown in Figure 2b, albeit with a small increase in RMS roughness from 0.3 nm to 1.2 nm. Low-magnification optical images and scanning electron microscope (SEM) images (Figure S10, Supporting Information) showed no evidence of bending-induced wear or damage on the macroscale, e.g. large wrinkles, cracks, or tears.
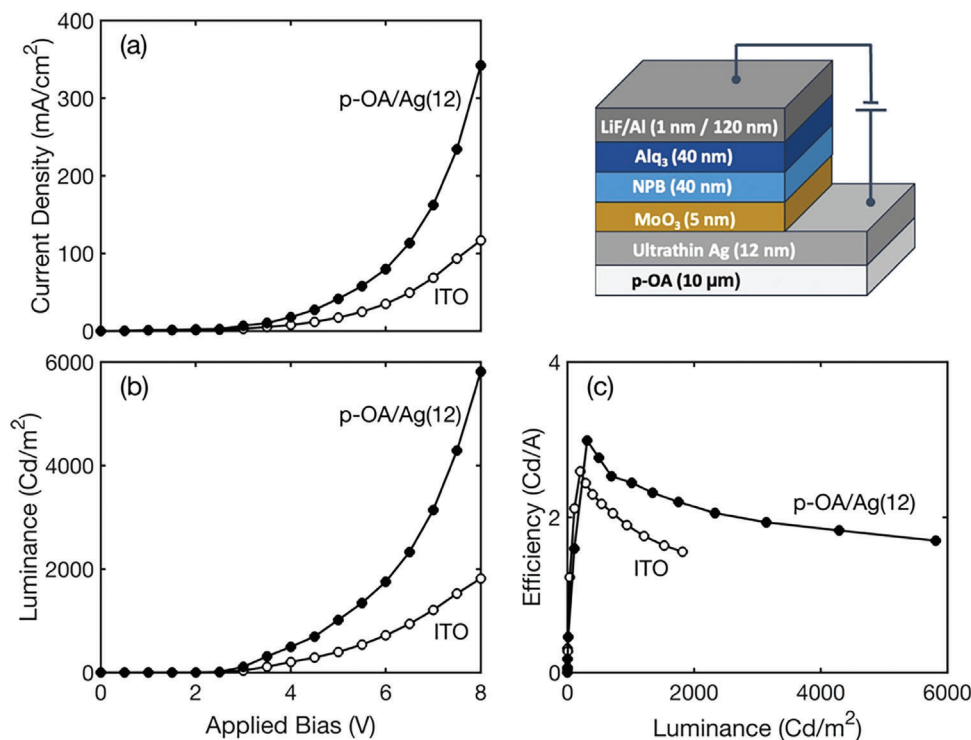
**ADVANCED
SCIENCE NEWS**

www.advancedsciencenews.com

**ADVANCED
MATERIALS**

www.advmat.de

Figure 6. a) Current density and b) luminance versus applied bias for NPB/Alq$_3$ organic light-emitting diodes based on a p-OA/Ag(12) anode (closed circles) or a glass/ITO anode with $\bar{T} = 83\%$ and $\mathcal{R}_s = 20\ \Omega$ sq^{-1}. The corresponding external quantum efficiency versus luminance data are shown in (c). The structure of the p-OA/Ag(12) device is shown inset, with the ITO device having an identical structure except for the replacement of glass/OTS/p-OA/Ag(12) by glass/ITO.

Higher magnification 14 µm × 10 µm SEM images taken after 0, 10, and 2000 bending cycles at a bending diameter of 3 mm are shown in Figure S11a-c, Supporting Information. Prior to bending, the pOA/Ag(12) film appears uniform with no obvious asperities in the SEM image. After 10 and 2000 bends, some faint streaks are evident in the SEM images but it is difficult to discern the cause due to the low image contrast. To better visualize the effects of bending, the three images were subjected to noise reduction and contrast enhancement (see caption to Figure S11, Supporting Information for details). The processed image of the unbent sample showed no signs of surface asperities, while the processed image of the sample after 10 bends showed clear cracks of typical length 2 µm and typical width < 40 nm, indicating the occurrence of microscale bending-induced damage after only a small number of bending cycles. The processed image of the same sample after 2000 bends was strikingly similar, showing microcracks of comparable length, width, and spacing to those observed after 10 bends. Hence, it is evident that the cracks formed in the early stages of bending are of a stable, nonpropagating nature and do not substantially increase in size or density under extended bending. The stable nature of the microcracks is attributable to the strong adhesion between the thiol atoms of NOA63 and silver, which prevents crack growth in both the axial and transverse directions. We speculate that the initial cracks may correspond to regions where local imperfections in the NOA63 substrate have resulted in poor adhesion to the evaporated silver atoms, resulting in rapid delamination when the substrate is first flexed. Hence, apart from a modest increase in sheet resis-

tance on initial bending, the p-OA/Ag samples otherwise show excellent resilience to mechanical flexing, making them attractive candidates for flexible TEs.

Figure 5d-f shows for comparison the effects of the same bending procedures on commercially sourced ITO films on PET. Subjecting the ITO films to single bends of $D_b = 30$ and 20 mm had no appreciable effect on the measured sheet resistance, which remained close to the 72 Ω sq^{-1} sheet resistance of an unbent ITO film. Further decreases in the bending diameter, however, resulted in a substantial increase in the sheet resistance, with $\mathcal{R}_s$ increasing to almost 2800 Ω sq^{-1} at a bending diameter of 1 mm. Repeated bending cycles at a fixed bending diameter of 3 mm similarly led to a rapid increase in sheet resistance, with $\mathcal{R}_s$ reaching more than 18 MΩ sq^{-1} after 3000 bending cycles. Low magnification AFM, SEM and optical images obtained after bending showed that the formation of large cracks and undulations in the film was responsible for the irreversible increase in sheet resistance (Figure S12, Supporting Information).

The OA/Ag TEs have many potential applications in flexible electronics. **Figure 6** shows illustrative data for a simple organic light-emitting diode (OLED) based on the well-studied N,N′-bis(1-naphthyl)-N,N′-diphenyl-1,1′-biphenyl-4,4′-diamine (NPB) / tris(8-hydroxy-quinoline)aluminum (Alq3) bilayer geometry, using MoO$_x$-coated OA/Ag(12) as the anode and LiF/Al as the cathode, see inset. The OA/Ag electrode was patterned (via selective etching of the OA layer) as a single 2-mm-wide stripe running the full 20-mm length of the substrate, while the Al electrode was patterned into a series of four 2-mm-wide stripes run-

ning the full 15-mm width of the substrate, yielding a pixel area of 4 mm^2 (see Figure S8d, Supporting Information). Figure 6a-c shows the current density versus voltage, the luminance versus voltage, and the external quantum efficiency versus luminance for a p-OA/Ag(12)/MoO$_x$/NPB/Alq$_3$/LiF/Al OLED, together with comparative data for an equivalent ITO/MoO$_x$/NPB/Alq$_3$/LiF/Al device. The $\bar{T}$ and $\mathcal{R}_s$ values for the p-OA/Ag(12) electrode were 59% and 16 Ω sq^{-1} compared to 83% and 20 Ω sq^{-1} for the glass/ITO electrode. Above turn-on ($V > 2.5$ V), current densities and luminances for the p-OA/Ag-based device were two to three times higher than for the ITO-based device. And, despite the lower transmittance of the p-OA /Ag electrode, the 1000 cd m^{-2} external quantum efficiency was ≈26% higher at 2.4 cd/A (cf. 1.9 cd/A for the ITO-based device). The maximum luminance of the p-OA/Ag-based device was 5816 cd m^{-2} compared to 1818 cd m^{-2} for the ITO-based device. Hence, for the chosen application, the p-OA/Ag(12) TE appreciably outperformed a conventional glass/ITO-based electrode.

Finally, it has previously been shown that substantial improvements in the transparency of UTMF electrodes may be achieved by using antireflective dielectric layers above and/or below the metal layer.[17,20] The use of NOA63 as a templating substrate precludes the use of a dielectric underneath the metal film, but it is still possible to combine the OA/Ag electrodes with a dielectric overlayer to enhance transparency. In Figure S13, Supporting Information, we show transmittance spectra for p-OA/Ag(12) electrodes coated with Al$_2$O$_3$ dielectric layers of varying thickness $d_{Al_2O_3}$ from 0 to 60 nm. From 0 to 40 nm, a progressive increase in the average transmittance of the samples from 58.7% to 71.5% was observed, accompanied by a slight red-shift in the peak transmittance wavelength from 440 to 465 nm. Increasing $d_{Al_2O_3}$ from 40 nm to 50 nm caused a substantial change in the shape of the spectrum, with a further red-shift of the peak transmittance wavelength to 505 nm and an increase in the average transmittance to 73.2 % ($T = 79.0\%$ at 550 nm). Further increasing $d_{Al_2O_3}$ to 60 nm caused a further red-shift in the peak transmittance to 519 nm and a slight drop in the average transmittance to 72.6% ($T = 78.1\%$ at 550 nm). The dielectric coating also caused a modest increase in the sheet resistance of the electrode, with $\mathcal{R}_s$ increasing from 16 Ω sq^{-1} without Al$_2$O$_3$ to ≈30 Ω sq^{-1} at $d_{Al_2O_3} = 60$ nm due to the insulating nature of Al$_2$O$_3$. This increase in sheet resistance could be avoided by using an electron-transporting oxide such as ZnO in place of Al$_2$O$_3$.[20]

The increased transmittance provided by the dielectric overcoating comes at the expense of a reduction in flexibility. The p-OA/Ag(12)/Al$_2$O$_3$(60) electrodes showed fairly good resilience to bending at high bending diameters, with for instance the sheet resistance increasing from an initial value of 31 Ω sq^{-1} before bending to 65 Ω sq^{-1} after 2000 bending cycles at a bending diameter of 10 mm. However, at lower bending diameters, the electrodes were substantially less resilient, with for instance $\mathcal{R}_s$ increasing from 27 Ω sq^{-1} before bending to 200 Ω sq^{-1} after 2000 bending cycles at a bending diameter of 3 mm. In contrast to the behavior of the p-OA/Ag(12) electrode reported in Figure 5b (and reproduced in blue in Figure S14a, Supporting Information), it can be seen that the sheet resistance of the p-OA/Ag(12)/Al$_2$O$_3$(60) electrode did not stabilize after the first few bending cycles, but increased steadily throughout the bending procedure. SEM images taken before (Figure S14b,c, Supporting

Information) and after (Figure S14c,d, Supporting Information) bending revealed the existence of long bending-induced cracks in the MD electrodes perpendicular to the tensile direction that extended over several millimeters. For the lower bending diameter of 3 mm, additional cracks were also observed at a small angle to the tensile direction as a presumed consequence of buckling.[41] High-magnification AFM images before and after bending are shown in Figure S15, Supporting Information.

Figures S16a,b, Supporting Information shows the sheet-resistance versus temperature for p-OA/Ag(12)/Al$_2$O$_3$(50) and e-OA/ Ag(12)/Al$_2$O$_3$(50) samples, measured under ambient conditions. The p-OA/Ag/Al$_2$O$_3$ samples showed a small increase in sheet-resistance from 32 to 50 Ω sq^{-1}. as the temperature was increased from 25 to 100 °C, suggesting slight oxidation of the silver. The e-OA/Ag/Al$_2$O$_3$ samples showed a sheet resistance of > 25 MΩ for temperatures up to 80 °C, before dropping to ≈38 kΩ sq^{-1} at a temperature of 100 °C due to a change in the surface morphology of the NOA63. AFM images of uncoated e-OA obtained before and after annealing at 100 °C indicate a loss of nanoscale structuring after annealing (see Figure S17, Supporting Information), with the RMS surface roughness of the NOA63 decreasing from 11.8 nm to 0.3 nm.

Figures S16c,d, Supporting Information shows the sheet-resistance versus annealing time for p-OA/Ag/Al$_2$O$_3$ and e-OA/Ag/Al$_2$O$_3$ samples, obtained at a fixed annealing temperature of 80 °C. The samples maintained their respectively low and high sheet resistances over the 24-hour duration of the measurement, indicating good stability at temperatures of up to 80 °C. This is broadly consistent with the manufacturer's guidelines for NOA63, which recommend an upper limit of 90 °C when it is used as a film or coating. For applications requiring tolerance to higher temperatures, NOA63 may be replaced by NOA61, which has a similar (thiolene-based) chemical formulation but is specified for use at temperatures of up to 125 °C. (Preliminary testing indicates that p-OA/Ag(12) and e-OA/Ag(12) samples prepared from NOA61 behave in a similar way to those prepared from NOA63, although a longer oxygen plasma treatment of at least 20 min is required to render the e-OA/Ag samples highly insulating).

3. Conclusions

We have fabricated flexible TEs formed from ultrathin (< 20 nm) films of silver on top of the commercial optical adhesive, Norland Optical Adhesive 63 (NOA63). Electron-beam deposition of 12 nm silver onto pristine NOA63 yielded ultrasmooth films ($\mathfrak{R} = 0.3$ nm) with fairly high average transmittances across the visible spectrum (59%) and low sheet resistances (16 Ω sq^{-1}), while deposition onto oxygen plasma etched NOA63 yielded rougher ($\mathfrak{R} = 7.5$ nm), fragmented films with reduced transmittances (44%) and extremely high sheet resistances (> 8.2×10^6 Ω sq^{-1}). By selectively treating the NOA63 with an oxygen plasma prior to silver deposition, insulating areas were introduced into an otherwise conducting silver film, creating a differentially conductive silver film that could serve as a TE for optoelectronics. Deliberately inducing differential conductivity in an ultrathin metal film is an attractive approach to fabricating patterned TEs that is simpler and easier to implement than conventional methods such as shadow-mask evaporation and photolithography. The use of

ADVANCED
SCIENCE NEWS

www.advancedsciencenews.com

ADVANCED
MATERIALS

www.advmat.de

differentially conductive silver as a patterned electrode may be of particular interest in bioelectronics, where the antibacterial properties of silver can be expected to prevent biofouling compared to a traditionally patterned electrode with regions of exposed substrate.

The patterned NOA63/Ag electrodes were readily detached from a supporting glass substrate to yield robust, flexible, freestanding TEs that could be repeatedly bent without significantly impairing their electrical characteristics. The transmittances of the electrodes could be further enhanced by adding a dielectric overlayer of Al_2O_3 on top of the silver. With 50 nm of Al_2O_3 an enhanced average visible light transmittance of 73.2% was obtained at the expense of an increase in sheet-resistance to 32 Ω sq^{-1} and a reduction in resilience to flexing. (Use of a conductive oxide such as ZnO in place of Al_2O_3 would avoid the observed increase in sheet-resistance).

On the basis of their T versus $\mathcal{R}_s$ trade-off characteristics, potential uses of the OA/Ag and OA/Ag/oxide TEs in their current form include photodetectors, thermotherapy pads, and transparent heaters, especially for applications requiring high flexibility such as wearable electronics. In addition, there is substantial scope for further optimizing the trade-off characteristics of the OA/Ag films through the use of metallic seed layers and/or metal doping of the silver films.[19,42] The successful application of seeding/doping to NOA/Ag films to increase transmittance substantially above 80% (at sheet resistances of a few tens of Ohms per square) would open up the full range of TE applications – including lighting, displays, and solar cells – while still providing high resilience to flexing and the convenience of patterning by O_2 plasma treatment of the OA layer.

Supporting Information

Supporting Information is available from the Wiley Online Library or from the author.

Conflict of Interest

The authors declare no conflict of interest.

Data Availability Statement

The data that support the findings of this study are available from the corresponding author upon reasonable request.

Keywords

flexible electrodes, microfabrication, patterning, transparent conductors, ultrathin silver

[1] T. Wang, K. Lu, Z. Xu, Z. Lin, H. Ning, T. Qiu, Z. Yang, H. Zheng, R. Yao, J. Peng, *Crystals* **2021**, *11*, 511.

[2] T. Sekitani, U. Zschieschang, H. Klauk, T. Someya, *Nat. Mater.* **2010**, *9*, 1015.

[3] H. G. Manning, C. G. da Rocha, C. O. Callaghan, M. S. Ferreira, J. J. Boland, *Sci. Rep.* **2019**, *9*, 11550.

[4] D. Baierl, B. Fabel, P. Lugli, G. Scarpa, *Org. Electron.* **2011**, *12*, 1669.

[5] A. Pierre, I. Deckman, P. B. Lechêne, A. C. Arias, *Adv. Mater.* **2015**, *27*, 6411.

[6] R. Rösch, D. M. Tanenbaum, M. Jørgensen, M. Seeland, M. Bärenklau, M. Hermenau, E. Voroshazi, M. T. Lloyd, Y. Galagan, B. Zimmermann, U. Würfel, M. Hösel, H. F. Dam, S. A. Gevorgyan, S. Kudret, W. Maes, L. Lutsen, D. Vanderzande, R. Andriessen, G. Teran-Escobar, M. Lira-Cantu, A. Rivaton, G. Y. Uzunoğlu, D. Germack, B. Andreasen, M. V. Madsen, K. Norrman, H. Hoppe, F. C. Krebs, *Energy Environ. Sci.* **2012**, *5*, 6521.

[7] W. Lan, Y. Chen, Z. Yang, W. Han, J. Zhou, Y. Zhang, J. Wang, G. Tang, Y. Wei, W. Dou, Q. Su, E. Xie, *ACS Appl. Mater. Interfaces* **2017**, *9*, 6644.

[8] S. Ullah, X. Yang, H. Q. Ta, M. Hasan, A. Bachmatiuk, K. Tokarska, B. Trzebicka, L. Fu, M. H. Rummeli, *Nano Res.* **2021**, *14*, 3756.

[9] E. Mullen, M. A. Morris, *Nanomaterials* **2021**, *11*, 1085.

[10] A. Kumar, C. Zhou, *ACS Nano* **2010**, *4*, 11.

[11] A. I. Hofmann, E. Cloutet, G. Hadziioannou, *Adv. Electron. Mater.* **2018**, *4*, 1700412.

[12] N. K., C. S. Rout, *RSC Adv.* **2021**, *11*, 5659.

[13] S. S. Siwal, A. K. Saini, S. Rarotra, Q. Zhang, V. K. Thakur, *J. Nanostruct. Chem.* **2021**, *11*, 93.

[14] P. Mustonen, D. M. A. Mackenzie, H. Lipsanen, *Front Optoelectron* **2020**, *13*, 91.

[15] M. Azani, A. Hassanpour, T. Torres, *Adv. Energy Mater.* **2020**, *10*, 2002536.

[16] J. Yun, *Adv. Funct. Mater.* **2017**, *27*, 1606641.

[17] M. Girtan, B. Negulescu, *Opt. Mater.: X* **2022**, *13*, 100122.

[18] I. Lee, J.-L. Lee, *J. Photon. Energy* **2015**, *5*, 057609.

[19] C. Zhang, Q. Huang, Q. Cui, C. Ji, Z. Zhang, X. Chen, T. George, S. Zhao, L. J. Guo, *ACS Appl. Mater. Interfaces* **2019**, *11*, 27216.

[20] C. Ji, D. Liu, C. Zhang, L. J. Guo, *Nat. Commun.* **2020**, *11*, 3367.

[21] S. Lee, L. J. Guo, *ACS Appl. Mater. Interfaces* **2022**, *14*, 7440.

[22] Y. H. Lee, I. Shabbir, K. H. Yoo, T. W. Kim, *Nano Energy* **2021**, *85*, 105975.

[23] M. Nazim, J. H. Kim, *ACS Appl. Nano Mater.* **2020**, *3*, 2322.

[24] Y.-H. Duan, Y. Duan, X. Wang, D. Yang, Y.-Q. Yang, P. Chen, F.-B. Sun, K.-W. Xue, Y. Zhao, *Appl. Surf. Sci.* **2015**, *351*, 445.

[25] S. Nam, M. Song, D.-H. Kim, B. Cho, H. M. Lee, J.-D. Kwon, S.-G. Park, K.-S. Nam, Y. Jeong, S.-H. Kwon, Y. C. Park, S.-H. Jin, J.-W. Kang, S. Jo, C. S. Kim, *Sci. Rep.* **2014**, *4*, 4788.

[26] M. Choi, J. W. Leem, J. S. Yu, *RSC Adv.* **2015**, *5*, 84865.

[27] S. W. Jin, Y. H. Lee, K. M. Yeom, J. Yun, H. Park, Y. R. Jeong, S. Y. Hong, G. Lee, S. Y. Oh, J. H. Lee, J. H. Noh, J. S. Ha, *ACS Appl. Mater. Interfaces* **2018**, *10*, 30706.

[28] K. Du, J. Ding, Y. Liu, I. Wathuthanthri, C.-H. Choi, *Micromachines* **2017**, *8*, 131.

[29] H. Yun, S. Kim, H. Kim, J. Lee, K. McAllister, J. Kim, S. Pyo, J. Sung Kim, E. E. B. Campbell, W. Hyoung Lee, S. Wook Lee, *Sci. Rep.* **2015**, *5*, 10220.

[30] J. Siegel, M. Polívková, M. Staszek, K. Kolářová, S. Rimpelová, V. Švorčík, *Mater. Lett.* **2015**, *145*, 87.

ADVANCED
SCIENCE NEWS

www.advancedsciencenews.com

ADVANCED
MATERIALS

www.advmat.de

[31] B. Gu, D. Ko, S. Jo, D. C. Hyun, H.-J. Oh, J. Kim, *Materials* **2020**, *13*, 3852.

[32] M. Atsuta, H. Matsumura, T. Tanaka, *J Prosthet Dent* **1992**, *67*, 296.

[33] E. Kuusisto, J. J. Heikkinen, P. Järvinen, T. Sikanen, S. Franssila, V. Jokinen, *Sens. Actuators, B* **2021**, *336*, 129727.

[34] M. Gholipour Shahraki, H. Savaloni, *Phys. Stat. Sol.* **2007**, *244*, 3115.

[35] N. Boysen, T. Hasselmann, S. Karle, D. Rogalla, D. Theirich, M. Winter, T. Riedl, A. Devi, *Angew. Chem., Int. Ed.* **2018**, *57*, 16224.

[36] G. B. Smith, A. I. Maaroof, M. B. Cortie, *Phys. Rev. B* **2008**, *78*, 165418.

[37] A. A. Earp, G. B. Smith, *J. Phys. D: Appl. Phys.* **2011**, *44*, 255102.

[38] G. B. Smith, A. A. Earp, *Nanotechnology* **2010**, *21*, 015203.

[39] Y. Park, C. Jeong, L. J. Guo, *Adv. Electron. Mater.* **2022**, *8*, 2100970.

[40] T. W. Phillips, J. C. de Mello, *Org. Electron.* **2013**, 139.

[41] F. Toth, F. G. Rammerstorfer, M. J. Cordill, F. D. Fischer, *Acta Mater.* **2013**, *61*, 2425.

[42] Z. Wang, X. Yang, Z. Yang, W. Guo, L. Lin, N. Li, E. Jiang, J. Zhang, B. Yan, J. Ye, *Front. Mater.* **2019**, *6*, 18.